Article

SnO$_2$ Nanowire/MoS$_2$ Nanosheet Composite Gas Sensor in Self-Heating Mode for Selective and ppb-Level Detection of NO$_2$ Gas

Jin-Young Kim [1], Ali Mirzaei [2,*] and Jae-Hun Kim [1,*]

[1] Department of Materials Science and Engineering, Inha University, Incheon 22212, Republic of Korea; piadote@naver.com

[2] Department of Materials Science and Engineering, Shiraz University of Technology, Shiraz 71557-13876, Iran

* Correspondence: mirzaei@sutech.ac.ir (A.M.); jaehun@inha.ac.kr (J.-H.K.)

Abstract: The development of low-cost and low-power gas sensors for reliable NO$_2$ gas detection is important due to the highly toxic nature of NO$_2$ gas. Herein, initially, SnO$_2$ nanowires (NWs) were synthesized through a simple vapor–liquid–solid growth mechanism. Subsequently, different amounts of SnO$_2$ NWs were composited with MoS$_2$ nanosheets (NSs) to fabricate SnO$_2$ NWs/MoS$_2$ NS nanocomposite gas sensors for NO$_2$ gas sensing. The operation of the sensors in self-heating mode at 1–3.5 V showed that the sensor with 20 wt.% SnO$_2$ (SM-20 nanocomposite) had the highest response of 13 to 1000 ppb NO$_2$ under 3.2 V applied voltage. Furthermore, the SM-20 nanocomposite gas sensor exhibited high selectivity and excellent long-term stability. The enhanced NO$_2$ gas response was ascribed to the formation of n-n heterojunctions between SnO$_2$ NWs and MoS$_2$, high surface area, and the presence of some voids in the SM-20 composite gas sensor due to having different morphologies of SnO$_2$ NWs and MoS$_2$ NSs. It is believed that the present strategy combining MoS$_2$ and SnO$_2$ with different morphologies and different sensing properties is a good approach to realize high-performance NO$_2$ gas sensors with merits such as simple synthesis and fabrication procedures, low cost, and low power consumption, which are currently in demand in the gas sensor market.

Keywords: MoS$_2$ nanosheet; SnO$_2$ NWs; self-heating; NO$_2$ gas; sensing mechanism

1. Introduction

NO$_2$ is a highly dangerous gas emitted from industrial activities, fuel combustion, biomass burning, and electricity generation [1]. NO$_2$ can affect global air quality and human health [2]. Long-term exposure to parts per million (ppm) levels of NO$_2$ can cause infections in the respiratory tract and lungs. Asthma, tissue hypoxia, pulmonary edema, and cardiovascular disease are affected by the presence of NO$_2$ gas [3–5]. Additionally, NO$_2$ contributes to the formation of acid rain and reduces the visibility of atmospheric photochemical smog [6,7]. Therefore, the threshold limit for NO$_2$ gas is set at 3 ppm [8]. In addition to its toxic effects, NO$_2$ gas is also considered a biomarker of lung infections [9]. Thus, the detection of NO$_2$ gas is highly important from safety and health perspectives.

Semiconducting metal oxides are often used for the detection of toxic gases. However, they often need a high temperature to show their best sensing performance [10,11]. Transition metal dichalcogenides (TMDs) with a two-dimensional (2D) nanosheet (NS) nature have the general formula MX$_2$ (M = Mo or W; X = S, Se, or Te), in which the metal layers are sandwiched between two chalcogen layers [12,13]. They can be used in different applications as a gas adsorbent [14], microwave adsorbent [15], and gas sensor.

WS$_2$ [16], WSe$_2$ [17], MoS$_2$ [18], and MoSe$_2$ [19] are the most important TMDs for gas sensing studies. In particular, MoS$_2$ has features such as fast charge transfer, adjustable band gap, high carrier mobility, and large surface area owing to its 2D nature, making it a favorable TMD for gas sensing applications, particularly low- or room-temperature gas

sensing [20]. However, its sensing properties in pristine form are generally not adequate for the high standards of today's life. Accordingly, it can be decorated [21], doped [22], or composited with other materials [23,24] to enhance its sensing properties. In particular, composite fabrication leads to the formation of heterojunctions, which can provide an additional source of resistance modulation, ultimately leading to significant resistance modulation [25].

Semiconducting *n*-type SnO_2 (E_g = 3.37 eV) [26] has high electron mobility, high availability, ease of synthesis, high stability, and excellent gas sensing properties [27,28]. Accordingly, different morphologies of SnO_2-like nanoparticles (NPs) [29], nanorods [30], nanobelts [31], nanotubes [32], nanofibers [33], and nanowires (NWs) [34] have been used for the detection of various gases. Even though some room temperature SnO_2 gas sensors have been reported in the literature [35], SnO_2 gas sensors often require high temperatures to achieve their best performance.

Thus, SnO_2-MoS_2 nanocomposites are a good choice for gas sensing [36–39], combining the relatively good sensitivity of MoS_2 at room temperature (RT) with the high sensitivity of SnO_2 at higher temperatures, resulting in the realization of a room-temperature or relatively low-temperature gas sensor with good performance. For example, Bai et al. [40] reported the growth of vertically aligned MoS_2 on SnO_2 nanotubes for the room-temperature detection of NO_2 gas with a response of approximately 35 to 100 ppm NO_2 gas. In addition, polyaniline-MOS_2-SnO_2 nanotubes were reported as room-temperature ammonia gas sensors [41]. Wang et al. [42] used SnO_2 NPs-MoS_2 NSs for ammonia sensing at RT. Viet et al. [43] decorated MoS_2 NSs on SnO_2 NWs to detect and discriminate between CO, NH_3, and H_2 gases. Xu et al. [44] used MoS_2 NSs/SnO_2 nanotubes for the detection of trimethylamine at 200 °C. Han et al. reported a MoS_2 NSs-SnO_2 NPs composite gas sensor with an 18.7–5 ppm response of NO_2 gas at RT [45]. Anyway, less attention has been paid to the composites of SnO_2 NWs with MoS_2 NSs. SnO_2 NWs with strong intrinsic gas sensing features, high surface area, and one-dimensional (1D) nature, in combination with MoS_2 NSs, can generate numerous heterojunctions, which offer new opportunities for the detection of NO_2 gas. Additionally, the operation of gas sensors in self-heating conditions is a promising approach to not only significantly decrease the sensing temperature but also remarkably lower power consumption. Hence, self-heated sensors offer opportunities for application in places with limited energy access.

In this study, SnO_2 NWs were initially produced using a vapor–liquid–solid (VLS) growth mechanism, which is a simple, low-cost, and highly efficient method for the synthesis of metal oxide NWs [46]. Afterward, SnO_2 NWs (10, 20, and 30 wt.%) were composited with MoS_2 NSs. Overall, the synthesis procedure is highly cost-effective, and even large-scale synthesis is feasible for possible industrial applications. After different advanced characterizations, gas sensors were fabricated, and the sensor with 20 wt.% SnO_2 NWs revealed the highest response to NO_2 gas under 3.2 V in self-heating mode with parts per billion (ppb)-level detection ability, high selectivity, and long-term stability. The enhanced NO_2 gas sensing performance was mainly related to the formation of SnO_2-MoS_2 n-n heterojunctions and the high surface area of the nanocomposite. We believe that the optimal sensor developed in this study, with low power consumption, low synthesis cost, and high sensing performance, can be regarded as a potential choice for industrial and practical applications.

2. Materials and Methods

2.1. Starting Materials

Metallic Sn powders with high purity of 99.5% (Merck, <150 μm size, Darmstadt, Germany) were used for growth of SnO_2 NWs. Also, commercial MoS_2 NSs (ACS Material, 100–200 nm, Pasadena, CA, USA) were used to prepare the SnO_2/MoS_2 nanocomposites.

2.2. Synthesis of SnO$_2$ NWs and SnO$_2$ NWs/MoS$_2$ NS Composite

Networked SnO$_2$ NWs were synthesized via a VLS growth mechanism similar to that reported in a previous study [47]. First, high-purity metallic Sn powder was put in a crucible inside a tubular furnace. A SiO$_2$-grown (200 μm) Si substrate equipped Ti (50 nm)/Pt (200 nm) bi-electrode was placed within a short distance. Then, the temperature was gradually increased in the presence of flowing O$_2$ (10 sccm) and N$_2$ (300 sccm) gases, and SnO$_2$ NWs were grown at 900 °C for 15 min on the substrate (Figure 1a). The SnO$_2$ NWs were then scratched from the substrate (Figure 1b) to form a composite with MoS$_2$ NSs. To prepare the composite, 5 mg MoS$_2$ NSs were mixed with 10, 20, and 30 wt.% SnO$_2$ NWs (denoted as SM-10, SM-20, and SM-30, respectively) under magnetic stirring for 24 h (Figure 1c).
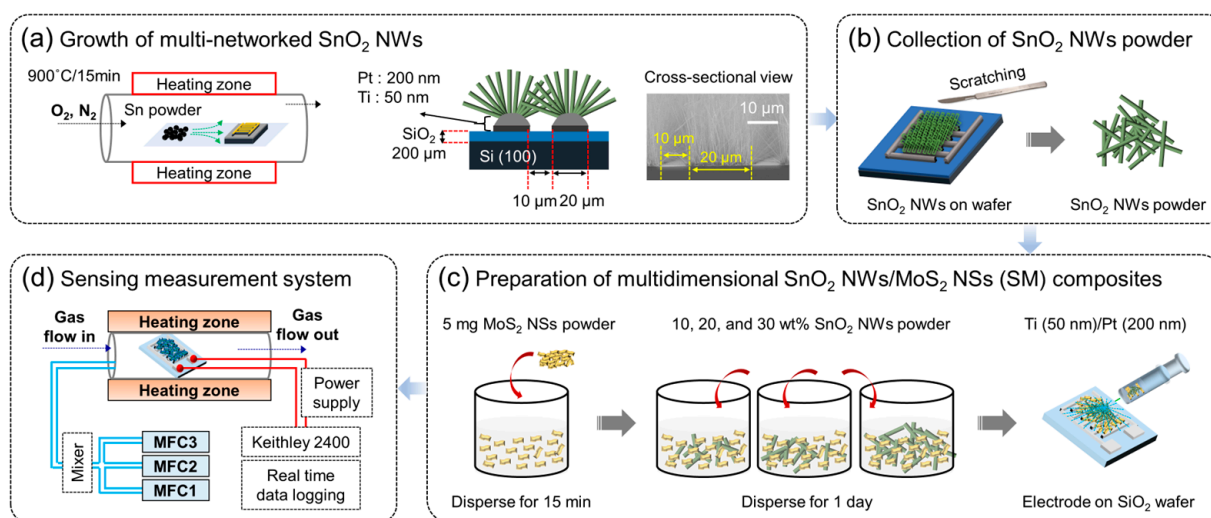
Figure 1. (**a**) Schematic of SnO$_2$ NWs grown via VLS mechanism on the surface of substrate equipped with electrodes. (**b**) Scratching of SnO$_2$ NWs for characterizations. (**c**) Preparation of SnO$_2$/MoS$_2$ composites. (**d**) Gas sensing measuring system.

2.3. Characterizations

Field-emission scanning electron microscopy (FE-SEM; Hitachi S-4200, Tokyo, Japan) and transmission electron microscopy (TEM; JEM2100F/JEOL, Tokyo, Japan) were used for morphological analysis. In FE-SEM, cold type was used as field emission gun with 15 kV power. X-ray photoelectron spectroscopy (XPS; K-Alpha/Thermo scientific, Seoul, Republic of Korea) was used for compositional analysis of the surface elements. Monochromated Al Kα was used as the X-ray source. The surface area was evaluated using the Brunauer–Emmett–Teller method (BET, MICROMERITICS Tristar, Norcross, GA, USA) from the N$_2$ adsorption–desorption isotherms. Induced temperature due to the Joule effect during the operation of the sensor in self-heating mode was monitored using a thermometer (IT-480S, Horiba, Kyoto, Japan). Ultraviolet photoemission spectroscopy (UPS, Thermo Fisher Scientific Co. Theta probe, Seoul, Republic of Korea) was used to estimate the work function values. He I (21.22 eV) was used as the light source.

2.4. Gas Sensing Tests

First, 5 mg of the sensing material was mixed with ethanol, and 0.075 μL of the solution (in three drops) was drop-coated onto the SiO$_2$ substrate equipped with Ti (50 nm)/Pt (200 nm) bi-layer electrodes (Figure 1c). Also, digital images of fabricated sensor are provided in Figure S1. A lab-made gas-sensing apparatus was used for the experiments (Figure 1d). The chamber was placed inside a tubular quartz furnace connected to a Keithley 2400 source meter. The gas was mixed with dry air and injected into the gas chamber using MFCs at a total flow rate of 100 sccm. The resistances in air (R_a) and in the presence of

the target gas (R_g) were measured constantly, and the sensor response was calculated as $R = R_g/R_a$ for NO_2 gas and vice versa for reducing gases. Additionally, the response time (τ_{res}) and recovery time (τ_{rec}) were defined as the times required for the resistance to reach its 90% final value after injection and stoppage of NO_2 gas, respectively [48]. During the gas sensing tests, the relative humidity (RH) in the chamber was 30% at RT. However, to evaluate the effect of higher humidity on the gas response, 80% RH was introduced into the gas chamber and measured at RT.

3. Results and Discussion

3.1. Characterization Studies

Figure S2a–c present low-magnification SEM images of pristine SnO_2, pristine MoS_2, and SM-20 nanocomposite samples, respectively. SnO_2 NWs are densely packed, while MoS_2 are loosely packed. Also, the SM-20 nanocomposite is comprised of both SnO_2 NWs and MoS_2 NSs with some voids among different components.

Figure 2a–c display SEM images of the SM-20 composite. In the high-magnification image (Figure 2a), the diameter of SnO_2 NWs is approximately 60–100 nm. Furthermore, in the lower-magnification images (Figure 2b,c), the formation of a nanocomposite comprising NSs and NWs is demonstrated. Due to the 1D morphology of SnO_2 NWs and 2D morphology of MoS_2 NSs, there are some voids among them, which are advantageous for the diffusion of gases. SEM-TEM EDS mapping analysis of different elements, namely Mo (panel i), S (panel ii), Sn (panel iii), and O (panel iv), shows that the composition of NSs is MoS_2 and the composition of NWs is SnO_2. SEM-EDS compositional analysis is presented in panel v of Figure 2. The amounts of Mo, S, Sn, and O elements were 21.92, 40.51, 12.15, and 25.42 at.%, respectively.
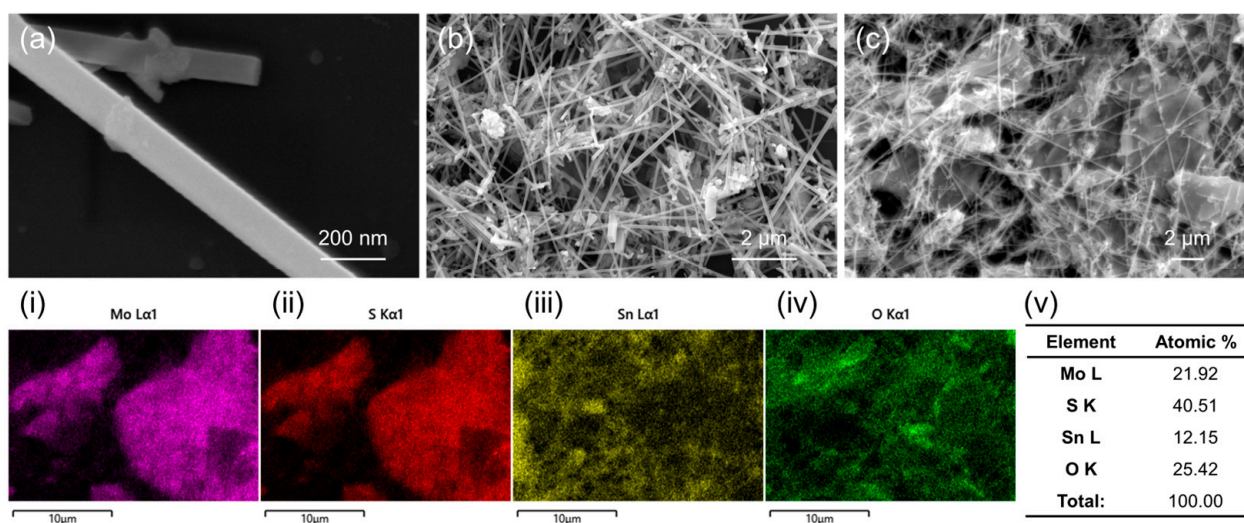

Figure 2. (**a**–**c**) SEM images of SM-20 composite. EDS mapping analysis of SM-20 composite: (**i**) Mo, (**ii**) S, (**iii**) Sn, and (**iv**) O mapping. (**v**) Compositional analysis of SM-20 composite.

Figure 3a,b show TEM views of the SM-20 nanocomposite at two different magnifications. Both MoS_2 NSs and SnO_2 NWs co-exist in the composite. High-resolution TEM (HRTEM) images of the SM-20 nanocomposite are shown in Figure 3c,d. The spacings between the parallel fringes are 0.335 and 0.27 nm, which correspond to (110) and (100) crystalline planes of SnO_2 and MoS_2, respectively [49,50]. TEM-EDS elemental mapping is presented in Figure 3e, panel i–iv. Based on the distribution of Sn, O, Mo, and S in panel i–iv of Figure 3, the NW morphology is mainly composed of Sn and O and, therefore, has a composition of SnO_2, whereas NSs have an MoS_2 composition. Figure S3a shows the XPS survey of the SM-20 composite. It shows the signals related to C (ambient carbon), Mo, S, Sn, and O, which demonstrates a high purity of the synthesized SM-20 composite.

Figure S3b displays the Mo 3d core-level region of the SM-20 composite, with two main peaks related to Mo $3d_{3/2}$ and Mo $3d_{5/2}$ at 233.1 and 229.9 eV, respectively, which can be attributed to Mo^{6+} ions in MoS_2 [51]. Additionally, a peak related to S 2s is observed near the Mo 3d peaks. Figure S3c manifests the S 2p core-level region of the SM-20 composite. It is comprised of S $2p_{1/2}$ and S $2p_{3/2}$ peaks, corresponding to S^{2-} ions in MoS_2 [52]. Figure S3d presents the Sn 3d core-level region of the SM-20 composite, where two high-intensity peaks at 495.5 and 487.1 eV with a separation of 8.4 eV belong to Sn $3d_{3/2}$ and Sn $3d_{5/2}$, respectively, in SnO_2 [53]. The O 1s core-level region is also presented in Figure S3e.
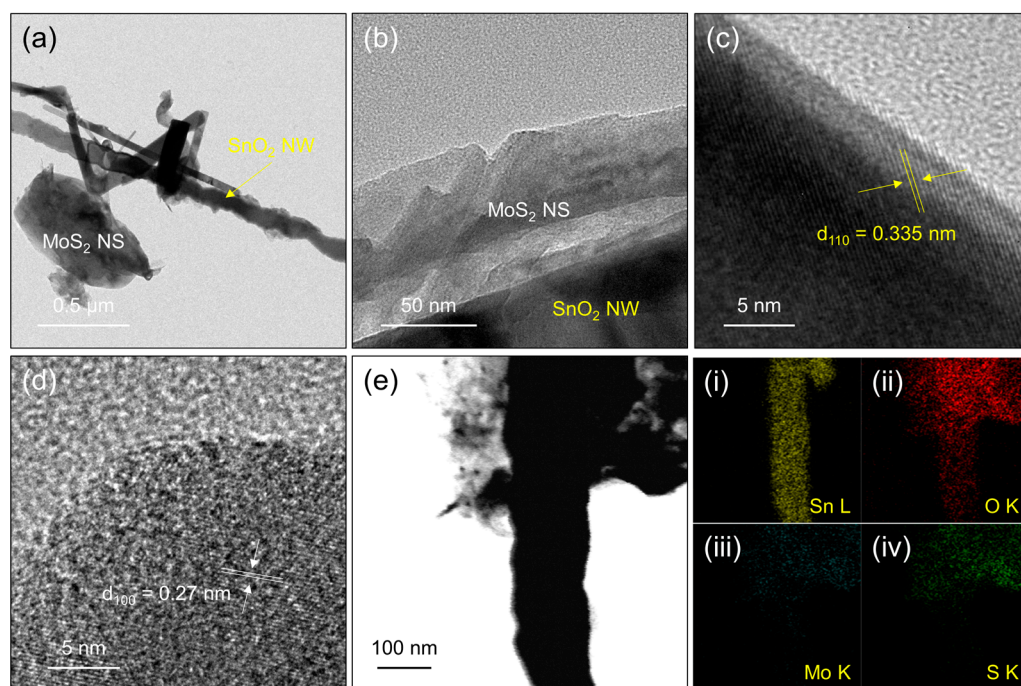
Figure 3. Analysis of SM-20 nanocomposite (**a**,**b**) TEM images at two different magnifications. (**c**,**d**) HRTEM images. (**e**) TEM-EDS elemental mapping analysis displaying the distribution of (**i**) Sn, (**ii**) O, (**iii**) Mo, and (**iv**) S elements.

Figure S4a–e display the N_2 adsorption–desorption curves of different samples. Based on these curves, the surface areas of the pristine MoS_2 and pristine SnO_2, SM-10, SM20, and SM-30 nanocomposites were samples were 0.65, 1.69, 2.14, 2.32, and 2.67 m^2/g, respectively. Therefore, after composite formation, the surface area increased by approximately four times relative to the MoS_2 NSs. In addition, it was approximately 1.4 times higher relative to the SnO_2 NWs. Thus, the composite sensors are expected to provide more adsorption sites for NO_2 gas and a higher response. Also, even though the SM-30 sample has a higher surface area relative to the SM-20 sample, it is expected to show a lower response due to the fact that in the SM-30 sample, more SnO_2 NWs are present, which have poorer sensing properties relative to MoS_2 at low temperatures.

3.2. Gas Sensing Studies

Figure S5a,b exhibit the dynamic resistance and dynamic response plots of the pristine MoS_2 NSs gas sensor to 1 ppm NO_2 at 25 °C (RH 30%) and higher temperatures (50–150 °C) under 1 V applied voltage, respectively. The resistance increased upon injection of the NO_2 gas, revealing the *n*-type nature of MoS_2. For better insight, the corresponding NO_2 gas response and baseline resistance versus operating temperature are depicted in Figure S5c. The baseline resistance gradually decreased with increasing temperature due to the jumping of electrons to the conduction band under the influence of temperature. This behavior demonstrates the semiconducting nature of the MoS_2 gas sensor. Furthermore, the tracking of response versus temperature shows that the highest response occurs at 100 °C, with a

response of 4.5–1 ppm NO_2 gas. At lower temperatures, there is insufficient energy for NO_2 gas to be sufficiently adsorbed on the sensor surface, and at higher temperatures, the desorption rate surpassed the adsorption rate. At 100 °C, maximum net adsorption occurs, resulting in enhanced gas response. Figure S5d,e show dynamic resistance and response plots of pristine SnO_2 NW gas sensors to 1 ppm NO_2 at 25 °C (RH 30%) and higher temperatures (50–350 °C) under 1 V applied voltage, respectively. Additionally, the corresponding NO_2 gas response and baseline resistance versus operating temperature are plotted in Figure S5f. Similar to the MoS_2 NSs gas sensor, the SnO_2 NWs gas sensor displays an *n*-type semiconducting behavior. However, its optimal sensing temperature was at 300 °C, with a high response of 38–1 ppm NO_2 gas. Therefore, although the optimal sensing temperature (100 °C) of the MoS_2 NSs sensor was lower relative to that of the SnO_2 NWs gas sensor (300 °C), the response of the SnO_2 NWs sensor (R_g/R_a = 38) was almost eight times that of the MoS_2 NSs gas sensor (R_g/R_a = 4.5). Conversely, at 100 °C, which is considered a low temperature for sensors, the response of the MoS_2 NSs sensor (R_g/R_a = 4.5) was more than four times higher than that of the SnO_2 NWs gas sensor (R_g/R_a = 1.05). This implies that to achieve high-performance gas sensors at low temperatures, the presence of only SnO_2 NWs is insufficient, and they should be used in combination with other materials, such as MoS_2, which have better sensing properties at low temperatures.

In the next step, we explored the NO_2 gas-sensing features of all fabricated gas sensors at 100 °C. Figure 4a displays the dynamic response curves of different gas sensors to 1 ppm NO_2 gas at 100 °C, and Figure 4b compares the response and baseline values of different gas sensors. The SnO_2 NWs gas sensor showed the lowest response of 1.05, whereas the response of the MoS_2 NSs gas sensor was 4.5. The responses of the SM-10, SM-20, and SM-30 sensors to 1 ppm NO_2 gas were 7.4, 11.8, and 10.7, respectively. Thus, all composite gas sensors exhibited a higher response than both the SnO_2 and MoS_2 gas sensors alone. In addition, among all gas sensors, the SM-20 composite exhibited the highest response; hence, it was selected for further study. In addition, the resistance of the gas sensors increased with increasing SnO_2 content, and pure MoS_2 and SnO_2 sensors exhibited the lowest and highest baseline resistances, respectively. Next, we exposed the SM-20 composite gas sensor to 1 ppm NO_2 gas at different applied voltages (1–3.5 V), as shown in Figure 5a. Figure 5b plots the response as a function of voltage. The response gradually increased with the applied voltage, and the maximum response occurred at 3.2 V. Thus, the optimal applied voltage was 3.2 V, and subsequent experiments were performed under this applied voltage.
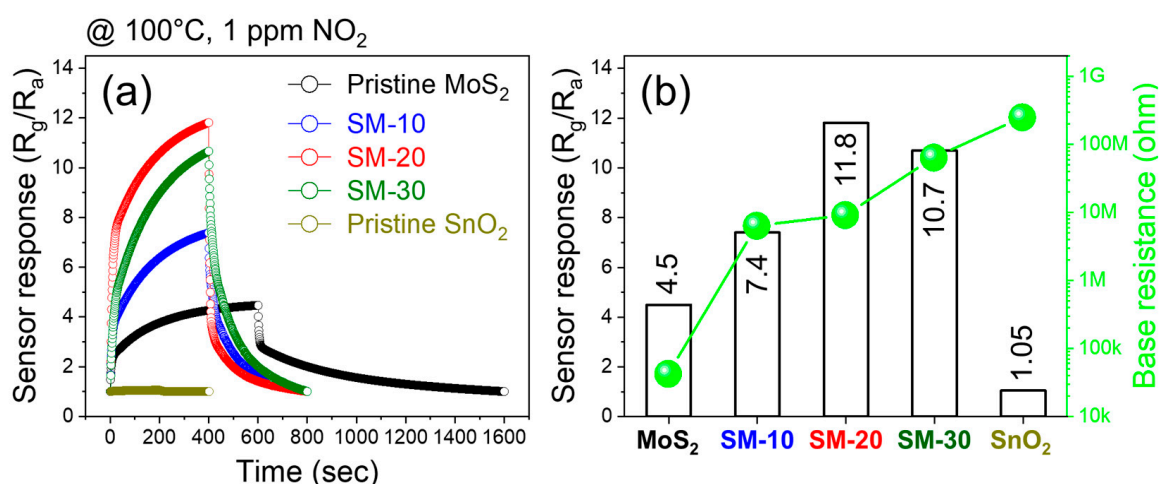
Figure 4. (**a**) Sensing curves of different gas sensors to 1 ppm NO_2 gas at 100 °C. (**b**) Comparison of response to 1 ppm NO_2 gas at 100 °C and baseline resistance of different gas sensors.
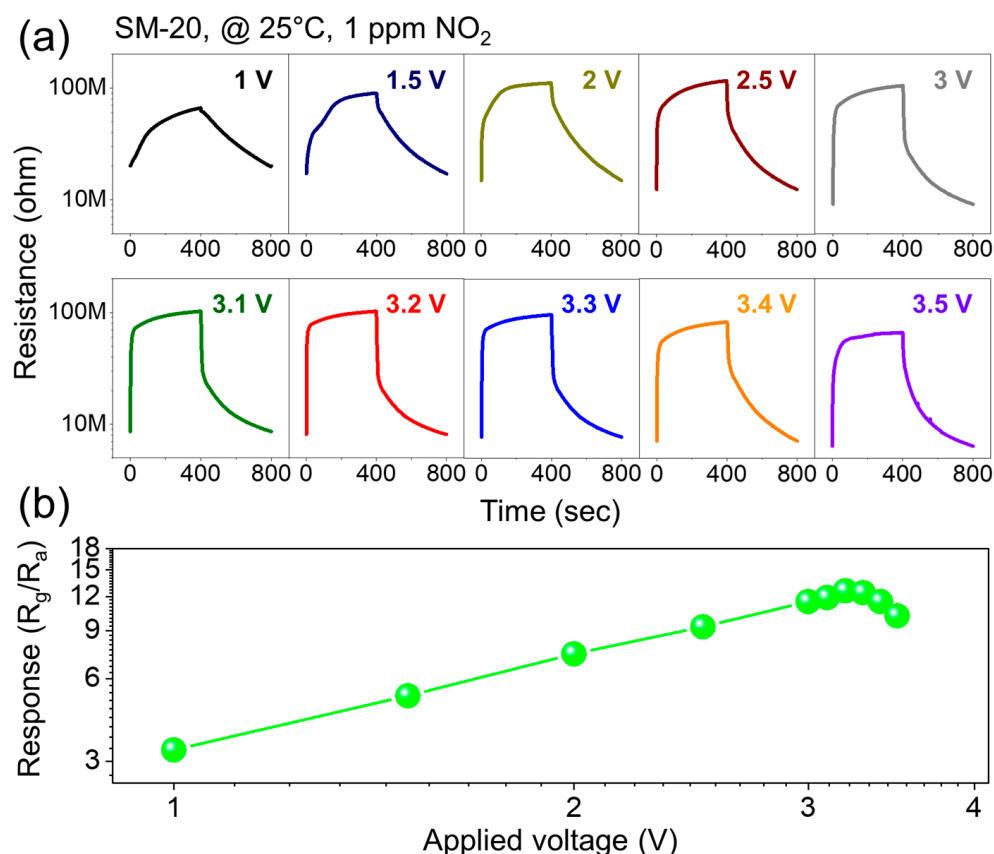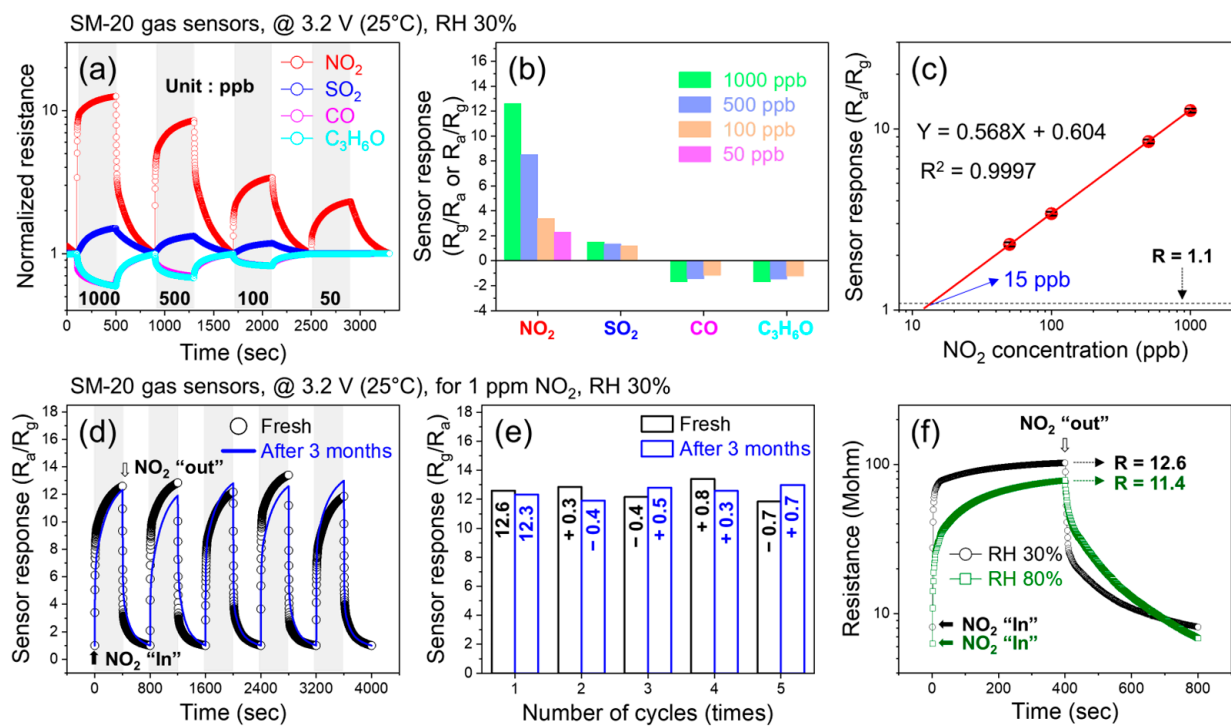
Figure 5. (**a**) Sensing curves of SM-20 gas sensor to 1 ppm NO$_2$ gas at 25 °C under various applied voltages. (**b**) Corresponding response of 1 ppm NO$_2$ gas at 25 °C versus applied voltage.

Figure 6a shows the dynamic normalized resistance curves of the SM-20 sensor at low concentrations of various gases at a fixed 3.2 V. The corresponding selectivity histogram is presented in Figure 6b. The responses to 1000 ppb NO$_2$, SO$_2$, CO, and C$_3$H$_6$O were 13, 2, 1.9, and 2, respectively. Thus, the sensor exhibited a much higher response to NO$_2$ gas than to other gases, demonstrating its high selectivity towards NO$_2$ gas. To check the reproducibility of the optimal sensor, we prepared three gas sensors under the same experimental procedures and checked their selectivity behavior, as shown in Figure S6a–c. All fabricated sensors revealed almost the same sensing response towards different gases, as shown in Figure S6d. Thus, the reproducibility of the sensor was demonstrated. In addition, the sensor exhibited a linear calibration curve for the detection of ppb levels of NO$_2$ gas (Figure 6c). Based on extrapolation to the y-axis, the experimental detection limit was 15 ppb, which was close to the theoretically calculated (Text S1 in Supporting Information) LOD (17.9). Figure 6d exhibits the sensing graphs (five cycles) of the SM-20 composite sensor in the fresh state and after three months of exposure to 1 ppm NO$_2$ gas at 3.2 V, and Figure 6e compares the responses in the fresh state and after three months. Overall, negligible differences were observed in the responses, even after three months. To be more quantitative, the average response and standard deviation of the sensor in the fresh state were 12.6 and 0.525, respectively, and those parameters for the sensor after three months were 12.52 and 0.386, respectively. If we define the stability factor as the average response after three months to the average response in the fresh state, it is 12.52/12.6 = 0.99. This demonstrates the good long-term stability of the sensor.

Finally, we explored the response of the SM-20 composite sensor at 80% RH (Figure 6f). The response to 1 ppm NO$_2$ gas at 3.2 V under dry conditions was 12.6, which decreased to 11.4 under humid (80% RH) conditions. Thus, although the response decreased in a humid environment, the sensor still exhibited a high response. In humid conditions, H$_2$O molecules are adsorbed on the sensor surface, limiting the number of available adsorption

sites. Therefore, a smaller amount of NO_2 gas can be adsorbed onto the sensor surface, bringing about a decrease in the sensor response in humid atmospheres [54].

Figure 6. Sensing performance of SM-20 gas sensor. (**a**) Sensing curves at low concentrations of various gases at fixed 3.2 V. (**b**) Corresponding selectivity histogram. (**c**) Calibration curve for low concentrations of NO_2 gas. (**d**) Dynamic resistance curves (five cycles) in fresh state and after three months of 1 ppm NO_2 gas at 3.2 V. (**e**) Comparison of the responses in fresh state and after three months. (**f**) Dynamic resistance curves for 1 ppm NO_2 gas at 3.2 V under dry and humid (80% RH) conditions.

Table 1 compares the NO_2 gas-sensing properties of present work with those obtained in other studies, which demonstrates good performance of present sensor.
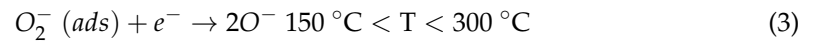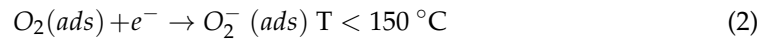
Table 1. Comparison of the NO_2 gas-sensing responses obtained in this study with those reported in other papers. The optimal sensor in this study has a higher performance in terms of high response, fast response, and recovery time relative to most of the listed sensors.

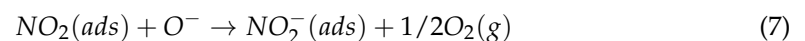| Sensing Material	T (°C)	Conc. (ppb)	Response (R_g/R_a) or (R_a/R_g)	τ_{Res}/τ_{Rec}	Ref.
SnO_2 NWs (20 wt%)-MoS_2 NSs composite gas sensor	RT, (3.2 V)	1000	12.6	268/63 s	This work
WS_2/Graphene heterostructure	RT	50	6.0	110/168 s	[55]
Nb-$MoSe_2$	150	3000	8.0	30/30 min	[56]
WSe_2 nanosheets	RT	1000	8.21	50/1050 s	[57]
MoS_2-rGO heterojunction	160	3000	1.24	8/20 s	[58]
Trilayer WSe_2 film	RT	10,000	2.8	960/600 s	[59]
3D crumpled reduced graphene oxide nanosheets	RT	1000	1.5	500/3000 s	[60]
SnO_2-rGO nanocomposites	50	500	1.5	400/300 s	[61]
SnO_2/$Ti_3C_2T_x$ nanocomposite	RT	300	78.2% [$\Delta R/R_a$ (%)]	54/400 s	[62]
ZnO/$Ti_3C_2T_x$ nanocomposite	160	8	3.6	254/~380	[63]
MoS_2/MXene nanocomposite	RT	100	65.6% [$\Delta R/R_a$ (%)]	~700/~900	[64]
MoS_2/$Ti_3C_2T_x$ nanocomposite	RT	20	65.6% [$\Delta R/R_a$ (%)]	525/155	[65]
$Ti_3C_2T_x$/CuO nanocomposite	RT	100	59% [$\Delta R/R_a$ (%)]	~100/~100	[66]

3.3. Gas-Sensing Mechanism

Initially, when the fresh sensors are in the air, oxygen gas is adsorbed on the sensor surface; because of the high electron affinity of oxygen, it takes electrons from the conduction band of the sensing material as follows [67].

$$O_2(g) \rightarrow O_2(ads) \tag{1}$$

$$O_2(ads) + e^- \rightarrow O_2^- \ (ads) \ \mathrm{T} < 150\,^{\circ}\mathrm{C} \tag{2}$$

$$O_2^- \ (ads) + e^- \rightarrow 2O^- \ 150\,^{\circ}\mathrm{C} < \mathrm{T} < 300\,^{\circ}\mathrm{C} \tag{3}$$

$$2O^- + e^- \rightarrow O^{2-} \ \mathrm{T} > 300\,^{\circ}\mathrm{C} \tag{4}$$

Hence, at room temperature and at 300 °C, dominant oxygen species are O_2^- and O^-, respectively. The depletion of electrons from the exposed surfaces of the sensing layer with *n*-type semiconducting nature leads to the appearance of an electron depletion layer (EDL), where the concentration of electrons is lower than that in the core regions, resulting in the high resistance of *n*-type sensors in air. Upon exposure to NO_2 gas, which is an oxidizing gas, more electrons are abstracted from the sensing layer as follows [8].

$$NO_2(g) \rightarrow NO_2(ads) \tag{5}$$

$$NO_2(ads) + e^- \rightarrow NO_2^-(ads) \tag{6}$$

$$NO_2(ads) + O^- \rightarrow NO_2^-(ads) + 1/2O_2(g) \tag{7}$$

Consequently, the EDL width increases in the presence of NO_2, which brings about the higher resistance of the sensor in the presence of NO_2 gas. However, both pristine SnO_2 and MoS_2 sensors revealed a low response at 100 °C due to limited sources of resistance modulation. All composite sensors exhibited a higher response to NO_2 than the pristine sensors, which could be related to the presence of *n-n* heterojunctions in the composite sensors. Figure 7a shows side views of MoS_2 NSs and the SM-20 composite on the substrate. In the composite sensor, it is expected that SnO_2 NWs bridge among MoS_2 NSs owing to the lower amount of SnO_2 NWs relative to MoS_2 NSs; hence, numerous *n-n* heterojunctions were created. Figure S7a presents the UPS spectra of the MoS_2 NSs and SnO_2 NWs. Based on energy-cut-off values and procedure reported in [68], the work functions of MoS_2 and SnO_2 were calculated to be 4.82 and 4.37 eV, respectively.
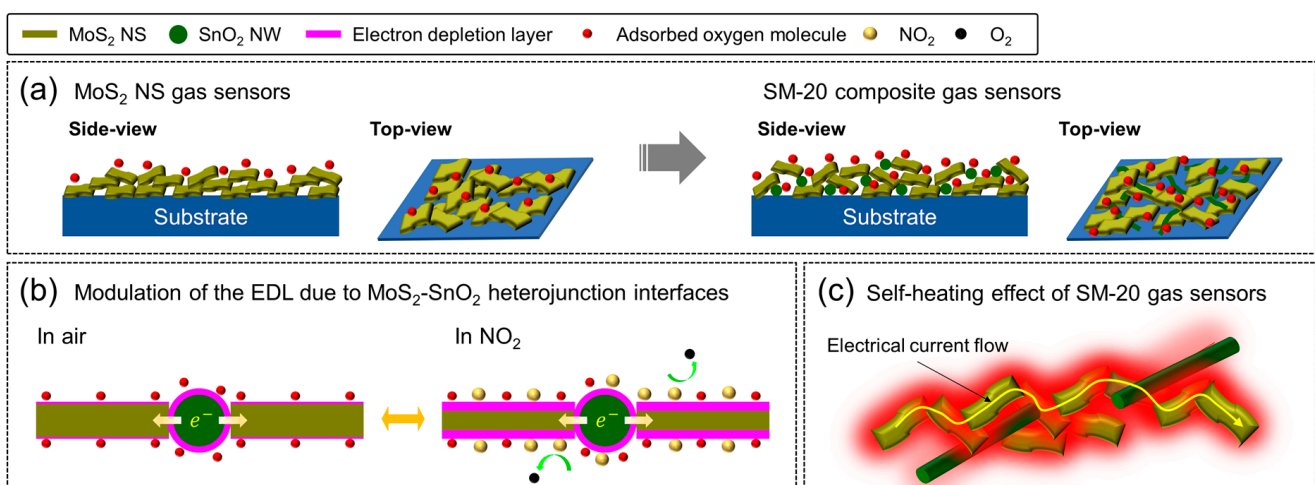
Figure 7. (**a**) Side views of MoS_2 NSs and SM-20 composite on the substrate. (**b**) Schematic of NO_2 gas sensing mechanism of SM-20 composite gas sensor. (**c**) Self-heating effect of SM-20 gas sensor.

Accordingly, we constructed their energy band levels, as shown in Figure S7b. Owing to the difference between the work functions of SnO_2 and MoS_2, upon intimate contact, the electrons were moved from SnO_2 to MoS_2 to equate the Fermi levels on both sides of the contact. This led to band bending and the formation of *n-n* heterojunction barriers in the air. Furthermore, due to the flow of electrons to MoS_2, which acts as the main sensing material, the thickness of the EDL on MoS_2 was smaller than that of the pristine MoS_2 sensor (Figure 7b). Accordingly, more electrons are available for extraction by NO_2 gas; hence, higher resistance modulation is expected. In addition, when the composite sensors were exposed to NO_2, more electrons were abstracted from the sensor surface, and the height of the heterojunction barriers further increased, which eventually led to an increase in resistance in the presence of NO_2 gas, contributing to the sensing signal. Thus, the presence of numerous heterojunctions in composite gas sensors is beneficial for NO_2 gas sensing. Therefore, the SM-20 composite exhibited a higher response than the SM-10 composite sensor.

However, a further increase in SnO_2 content decreased the sensor response, which could be related to the agglomeration of SnO_2 NWs, a decrease in the number of n-MoS_2/ n-SnO_2 heterojunctions, and a simultaneous increase in the number of SnO_2-SnO_2 homojunctions. Additionally, as the amount of SnO_2 is increased, the amount of MoS_2 NSs that are better sensing materials at 100 °C is simultaneously decreased. In other words, the contribution of SnO_2 NWs with interferer sensing response at 100 °C may be significant in the CM-30 nanocomposite sensor, resulting in a decrease in the overall performance. In addition to the formation of heterojunctions, the higher surface area of the composite gas sensors and the presence of voids between the SnO_2 NWs and MoS_2 NSs were beneficial for the diffusion and migration of NO_2 gas molecules. Owing to the combination of 1D SnO_2 NWs with 2D MoS_2 NSs, some voids were created among them, which acted as channels for the high diffusion of NO_2 gas into deeper parts of the sensor.

High selectivity to NO_2 gas can be related to (i) the high electron affinity of NO_2 gas (2.28 eV) compared to oxygen (0.43 eV), which can directly abstract electrons on the sensor surface, whereas other gases must react with adsorbed oxygen species to generate a sensing signal [69], (ii) the presence of N in NO_2 gas with an unpaired electron, which can bond with the sensor surface [70], and (iii) the relatively low bond energy of O–NO (305.0 kJ/mol) in NO_2, which improves the response to NO_2 [71].

During the operation of the gas sensors in self-heating mode, electrons accelerate owing to the application of voltage, and on their pathways, they lose their high kinetic energies as heat after collision with other electrons, ions, and atoms in a process known as the Joule heating effect. Figure S7a manifests the induced temperatures of the MoS_2 NSs, SnO_2 NWs, and SM-20 composite gas sensor versus applied voltage. Among them, the temperature of the SM-20 composite sensor was higher at a fixed applied voltage, demonstrating the presence of more sources of heat generation inside the sensor owing to the contact areas between the MoS_2 NSs and SnO_2 NWs, which acted as powerful sources of Joule heating (Figure 7c). Figure S7b shows the induced temperature of the SM-20 composite as a function of applied voltage in the range of 1–3.5 V. Under 1, 1.5, 2, 2.5, 3, 3.1, 3.2, 3.3, 3.4, and 3.5 V applied voltage, the induced temperature values were 38, 55, 71, 88, 106, 110, 114, 118, 122, and 126 °C, respectively. Therefore, under the optimal applied voltage of 3.2 V, a sufficiently high temperature was induced inside the sensor, which was sufficient to activate the adsorption and reaction of NO_2 gas on the sensor surface. Under optimal sensing temperature and voltage, the power consumption (V^2/R) of MoS_2 NSs (100 °C, 1 V), SnO_2 NWs (300 °C, 1 V), and SM-20 nanocomposite (RT, 3.2 V) sensors were calculated to be = 23.6, 0.2, and 1.3 µW, respectively. Despite the low power consumption of the SnO_2 NW gas sensor (0.2 µW), an increase in the temperature to 300 °C using external heating will result in significant power consumption, as an external heater is required to maintain this high temperature. For example, if an external heater uses 5 V to increase the sensor temperature to 300 °C, the power consumption will be 5.2 µW. Therefore, the SM-20 nanocomposite gas sensor showed the lowest power consumption in this study.

4. Conclusions

Briefly, we introduced self-heated NO_2 gas sensors based on SnO_2 NWs/MoS_2 NSs composites. SnO_2 NWs were synthesized via a VLS mechanism, and then 10, 20, and 30 wt.% SnO_2 NWs were composited with MoS_2 NSs. Different characterization techniques, such as SEM/TEM and EDS, demonstrated the formation of nanocomposites with desired compositions. Also, some voids were presented among NWs and NSs, which were beneficial for efficient gas diffusion. Different voltages were applied on the sensor electrodes in self-heating mode, and the SM-20 composite, with 20 wt% SnO_2 NWs, showed the highest response of 13 to 0.1 ppm NO_2 gas at 3.2 V applied voltage. Furthermore, the optimal sensor revealed selectivity, long-term stability, reproducibility, and repeatability. The improved sensing performance was attributed to the generation of n-SnO_2/n-MoS_2 heterojunctions, which acted as sources of resistance modulation, high surface area due to the NW and NS nature of SnO_2 and MoS_2 materials, respectively, along with the presence of voids in the SM-20 composite sensor. The present strategy, which combines the gas sensing properties of SnO_2 and MoS_2 with 1D and 2D morphologies, is a promising approach to boost the sensing features of the resultant gas sensor.

Supplementary Materials: The following supporting information can be downloaded at: https://www.mdpi.com/article/10.3390/chemosensors12060107/s1, Text S1: Calculation of limit of detection; Figure S1: (a,b) Digital images of fabricated sensor; Figure S2: SEM images of (a) SnO_2 NW, (b) MoS_2 NSs, and (c) SM-20 nanocomposite; Figure S3: (a) XPS survey of SM-20 composite. XPS core-level regions of (b) Mo 3d, (c) S 2p, (d) Sn 3d, and (e) O 1s; Figure S4: N_2 adsorption–desorption isotherms of (a) MoS_2 NSs, (b) SnO_2 NWs, (c) SM-10, (d) SM-20, and (e) SM-30 nanocomposite; Figure S5: Dynamic resistance and dynamic response plots of pristine MoS_2 NS gas sensor to 1 ppm NO_2 at (a) 25 °C and (b) different temperature (50–150 °C) under 1 V applied voltage. (c) Corresponding NO_2 gas response and baseline resistance versus operating temperature. Dynamic resistance plots of pristine SnO_2 NW gas sensors to 1 ppm NO_2 at (d) 25 °C and (e) different temperatures (50–350 °C) under 1 V applied voltage. (f) Corresponding NO_2 gas response and baseline resistance versus operating temperature; Figure S6. Reproducibility tests of three SM-20 gas sensors prepared under the same conditions. Sensing performance of SM-20 gas sensor (a) number 1, (b) number 2, and (c) number 3 (a) to low concentrations of various gases at fixed 3.2 V. (d) Corresponding selectivity histograms of three gas sensors; Figure S7: (a) UPS spectra and energy cut-off values of MoS_2 NSs and SnO_2 NWs. (b) Energy band levels of MoS_2 NSs and SnO_2 NWs before and after intimate contact; Figure S8: (a) Sensor temperature versus applied voltage for different gas sensors. (b) Temperature of SM-20 gas sensor versus applied voltage in the range of 1 to 3.5 V.

Author Contributions: Investigation, data curation, writing—original draft preparation, writing—review and editing, J.-Y.K.; writing—original draft preparation, writing—review and editing, supervision, A.M.; conceptualization, validation, formal analysis, investigation, writing—original draft preparation, writing—review and editing, visualization, supervision, funding acquisition, J.-H.K. All authors have read and agreed to the published version of the manuscript.

Institutional Review Board Statement: Not applicable.

Informed Consent Statement: Not applicable.

Data Availability Statement: Data will be made available upon request.

Conflicts of Interest: The authors declare no conflicts of interest.

References

1. Liu, F.; Zhang, L.; Zhang, C.; Chen, Z.; Li, J. Impact of NO_2 Emissions from Household Heating Systems with Wall-Mounted Gas Stoves on Indoor and Ambient Air Quality in Chinese Urban Areas. *Sci. Total Environ.* **2024**, *908*, 168075. [CrossRef]
2. Jion, M.M.M.F.; Jannat, J.N.; Mia, M.Y.; Ali, M.A.; Islam, M.S.; Ibrahim, S.M.; Pal, S.C.; Islam, A.; Sarker, A.; Malafaia, G.; et al. A Critical Review and Prospect of NO_2 and SO_2 Pollution over Asia: Hotspots, Trends, and Sources. *Sci. Total Environ.* **2023**, *876*, 162851. [CrossRef] [PubMed]

3. Bai, H.; Feng, C.; Guo, H.; Li, X.; Liu, W.; Feng, Y.; Liu, K.; Chen, D.; Zheng, Y.; Guo, F. UV-Activated CuO Nanospheres Modified with rGO Nanosheets for Ppb-Level Detection of NO_2 Gas at Room Temperature. *Sens. Actuators B Chem.* **2023**, *393*, 134195. [CrossRef]

4. Peng, H.; Yang, J.; Lin, C.; Qi, L.; Li, L.; Shi, K. Gas-Sensitive Performance of Metal-Organic Framework-Derived CuO $NPs/Ti_3C_2T_X$ MXene Heterostructures for Efficient NO_2 Detection at Room Temperature. *J. Alloys Compd.* **2024**, *980*, 173657. [CrossRef]

5. Gao, J.; Yin, Y.; Guo, Y.; Jia, L.; Xia, F.; Liu, C.; Hou, M.; Wang, F. Synthesis of $Ti_3C_2T_x$ Nanosheets / ZnO Nanowires Composite Material for NO_2 Gas Sensing. *Arab. J. Chem.* **2024**, *17*, 105776. [CrossRef]

6. Feng, Z.; Wang, H.; Zhang, Y.; Han, D.; Cheng, Y.; Jian, A.; Sang, S. ZnO/GaN n-n Heterojunction Porous Nanosheets for Ppb-Level NO_2 Gas Sensors. *Sens. Actuators B Chem.* **2023**, *396*, 134629. [CrossRef]

7. Brophy, R.E.; Junker, B.; Fakhri, E.A.; Árnason, H.Ö.; Svavarsson, H.G.; Weimar, U.; Bârsan, N.; Manolescu, A. Ultra Responsive NO_2 Silicon Nanowires Gas Sensor. *Sens. Actuators B Chem.* **2024**, *410*, 135648. [CrossRef]

8. Shin, K.Y.; Mirzaei, A.; Oum, W.; Kim, E.B.; Kim, H.M.; Moon, S.; Kim, S.S.; Kim, H.W. Enhanced NO_2 Gas Response of $ZnO–Ti_3C_2T_x$ MXene Nanocomposites by Microwave Irradiation. *Sens. Actuators B Chem.* **2024**, *409*, 135605. [CrossRef]

9. Mokrushin, A.S.; Gorban, Y.M.; Averin, A.A.; Gorobtsov, P.Y.; Simonenko, N.P.; Lebedinskii, Y.Y.; Simonenko, E.P.; Kuznetsov, N.T. Obtaining of ZnO/Fe_2O_3 Thin Nanostructured Films by AACVD for Detection of Ppb-Concentrations of NO_2 as a Biomarker of Lung Infections. *Biosensors* **2023**, *13*, 445. [CrossRef]

10. Qin, H.; Xie, J.; Xu, H.; Li, Y.; Cao, Y. Green Solid-State Chemical Synthesis and Excellent Xylene-Detecting Behaviors of Y-Doped α-MoO_3 Nanoarrays. *Mater. Res. Bull.* **2017**, *93*, 256–263. [CrossRef]

11. Hussain, S.; Amu-Darko, J.N.O.; Wang, M.; Alothman, A.A.; Ouladsmane, M.; Aldossari, S.A.; Khan, M.S.; Qiao, G.; Liu, G. CuO-Decorated MOF Derived ZnO Polyhedral Nanostructures for Exceptional H_2S Gas Detection. *Chemosphere* **2023**, *317*, 137827. [CrossRef] [PubMed]

12. Joseph, S.; Mohan, J.; Lakshmy, S.; Thomas, S.; Chakraborty, B.; Thomas, S.; Kalarikkal, N. A Review of the Synthesis, Properties, and Applications of 2D Transition Metal Dichalcogenides and Their Heterostructures. *Mater. Chem. Phys.* **2023**, *297*, 127332. [CrossRef]

13. Krishna, S.; Choi, S.H.; Kim, S.M.; Kim, K.K. Sapphire Substrates for Large-Area 2D Transition Metal Dichalcogenides Synthesis: A Brief Review. *Curr. Appl. Phys.* **2024**, *59*, 208–213. [CrossRef]

14. Guan, L.; Chen, Z.; Liu, Y.; Wang, R.; Yan, K.; Xu, Z.; Li, J.; Liu, Z.; Li, J.; Liu, H. Engineering Sulfur-Rich MoS_2 Adsorbent with Abundant Unsaturated Coordination Sulfur Sites for Gaseous Mercury Capture from High-Concentration SO_2 Smelting Flue Gas. *Chem. Eng. J.* **2024**, *483*, 149122. [CrossRef]

15. Yan, Y.; Zhang, K.; Qin, G.; Gao, B.; Zhang, T.; Huang, X.; Zhou, Y. Phase Engineering on MoS_2 to Realize Dielectric Gene Engineering for Enhancing Microwave Absorbing Performance. *Adv. Funct. Mater.* **2024**, *34*, 2316338. [CrossRef]

16. Yang, D.-H.; Kim, J.-H.; Mirzaei, A.; Kim, H.W.; Kim, S.S. Co-Decoration of WS_2 Nanosheets with Both Au and In_2O_3-Nanoparticles for Attaining the CO Sensing in Self-Heating Mode. *Appl. Surf. Sci.* **2023**, *635*, 157790. [CrossRef]

17. Wang, T.; Liu, G.; Zhang, D.; Wang, D.; Chen, F.; Guo, J. Fabrication and Properties of Room Temperature Ammonia Gas Sensor Based on SnO_2 Modified WSe_2 Nanosheets Heterojunctions. *Appl. Surf. Sci.* **2022**, *597*, 153564. [CrossRef]

18. Pramanik, M.; Jana, B.; Ghatak, A.; Das, K. Improvement in Efficiency of MoS_2 Nanoflower Based Ethylene Gas Sensor on Transition Metal Doping: An Experimental and Theoretical Investigation. *Mater. Chem. Phys.* **2024**, *314*, 128892. [CrossRef]

19. Kodan, S.; Kumar, A.; Sanger, A.; Arora, A.; Malik, V.K.; Chandra, R. Vertically Aligned $MoSe_2$-WS_2 Nanoworms Heterojunction towards Room Temperature NO_2 Gas Sensors. *Sens. Actuators B Chem.* **2024**, *407*, 135481. [CrossRef]

20. Kumar, S.; Mirzaei, A.; Kumar, A.; Lee, M.H.; Ghahremani, Z.; Kim, T.-U.; Kim, J.-Y.; Kwoka, M.; Kumar, M.; Kim, S.S.; et al. Nanoparticles Anchored Strategy to Develop 2D MoS_2 and $MoSe_2$ Based Room Temperature Chemiresistive Gas Sensors. *Coord. Chem. Rev.* **2024**, *503*, 215657. [CrossRef]

21. Chen, P.; Hu, J.; Yin, M.; Bai, W.; Chen, X.; Zhang, Y. MoS_2 Nanoflowers Decorated with Au Nanoparticles for Visible-Light-Enhanced Gas Sensing. *ACS Appl. Nano Mater.* **2021**, *4*, 5981–5991. [CrossRef]

22. Burman, D.; Raha, H.; Manna, B.; Pramanik, P.; Guha, P.K. Substitutional Doping of MoS_2 for Superior Gas-Sensing Applications: A Proof of Concept. *ACS Sens.* **2021**, *6*, 3398–3408. [CrossRef] [PubMed]

23. Le, V.T.; Vasseghian, Y.; Doan, V.D.; Nguyen, T.T.T.; Vo, T.-T.T.; Do, H.H.; Vu, K.B.; Vu, Q.H.; Lam, T.D.; Tran, V.A. Flexible and High-Sensitivity Sensor Based on Ti_3C_2–MoS_2 MXene Composite for the Detection of Toxic Gases. *Chemosphere* **2022**, *291*, 133025. [CrossRef] [PubMed]

24. Singh, S.; Sattigeri, R.M.; Kumar, S.; Jha, P.K.; Sharma, S. Superior Room-Temperature Ammonia Sensing Using a Hydrothermally Synthesized MoS_2/SnO_2 Composite. *ACS Omega* **2021**, *6*, 11602–11613. [CrossRef] [PubMed]

25. Miller, D.R.; Akbar, S.A.; Morris, P.A. Nanoscale Metal Oxide-Based Heterojunctions for Gas Sensing: A Review. *Sens. Actuators B Chem.* **2014**, *204*, 250–272. [CrossRef]

26. Hassun, H.K.; Hussein, B.H.; Salman, E.M.T.; Shaban, A.H. Photoelectric Properties of SnO_2: Ag/P–Si Heterojunction Photodetector. *Energy Rep.* **2020**, *6*, 46–54. [CrossRef]

27. Yamazoe, N.; Sakai, G.; Shimanoe, K. Oxide Semiconductor Gas Sensors. *Catal. Surv. Asia* **2003**, *7*, 63–75. [CrossRef]

28. Kong, Y.; Li, Y.; Cui, X.; Su, L.; Ma, D.; Lai, T.; Yao, L.; Xiao, X.; Wang, Y. SnO_2 Nanostructured Materials Used as Gas Sensors for the Detection of Hazardous and Flammable Gases: A Review. *Nano Mater. Sci.* **2022**, *4*, 339–350. [CrossRef]

29. Meng, X.; Bi, M.; Xiao, Q.; Gao, W. Ultra-Fast Response and Highly Selectivity Hydrogen Gas Sensor Based on Pd/SnO$_2$ Nanoparticles. *Int. J. Hydrogen Energy* **2022**, *47*, 3157–3169. [CrossRef]

30. Lee, J.H.; Park, M.S.; Jung, H.; Choe, Y.-S.; Kim, W.; Song, Y.G.; Kang, C.-Y.; Lee, H.-S.; Lee, W. Selective C$_2$H$_2$ Detection with High Sensitivity Using SnO$_2$ Nanorod Based Gas Sensors Integrated with a Gas Chromatography. *Sens. Actuators B Chem.* **2020**, *307*, 127598. [CrossRef]

31. Tan, Y.; Zhang, J. Highly Sensitive Ethanol Gas Sensors Based on Co-Doped SnO$_2$ Nanobelts and Pure SnO$_2$ Nanobelts. *Phys. E Low-Dimens. Syst. Nanostructures* **2023**, *147*, 115604. [CrossRef]

32. Su, P.; Li, W.; Zhang, J.; Xie, X. Chemiresistive Gas Sensor Based on Electrospun Hollow SnO$_2$ Nanotubes for Detecting NO at the Ppb Level. *Vacuum* **2022**, *199*, 110961. [CrossRef]

33. Phuoc, P.H.; Hung, C.M.; Toan, N.V.; Duy, N.V.; Hoa, N.D.; Hieu, N.V. One-Step Fabrication of SnO$_2$ Porous Nanofiber Gas Sensors for Sub-Ppm H$_2$S Detection. *Sens. Actuators Phys.* **2020**, *303*, 111722. [CrossRef]

34. Domènech-Gil, G.; Samà, J.; Fàbrega, C.; Gràcia, I.; Cané, C.; Barth, S.; Romano-Rodríguez, A. Highly Sensitive SnO$_2$ Nanowire Network Gas Sensors. *Sens. Actuators B Chem.* **2023**, *383*, 133545. [CrossRef]

35. Zhang, Y.; Jiang, Y.; Yuan, Z.; Liu, B.; Zhao, Q.; Huang, Q.; Li, Z.; Zeng, W.; Duan, Z.; Tai, H. Synergistic Effect of Electron Scattering and Space Charge Transfer Enabled Unprecedented Room Temperature NO$_2$ Sensing Response of SnO$_2$. *Small* **2023**, *19*, 2303631. [CrossRef] [PubMed]

36. Yang, Y.; Gong, W.; Li, X.; Liu, Y.; Liang, Y.; Chen, B.; Yang, Y.; Luo, X.; Xu, K.; Yuan, C. Light-Assisted Room Temperature Gas Sensing Performance and Mechanism of Direct Z-Scheme MoS$_2$/SnO$_2$ Crystal Faceted Heterojunctions. *J. Hazard. Mater.* **2022**, *436*, 129246. [CrossRef] [PubMed]

37. Yan, H.; Song, P.; Zhang, S.; Yang, Z.; Wang, Q. Dispersed SnO$_2$ Nanoparticles on MoS$_2$ Nanosheets for Superior Gas-Sensing Performances to Ethanol. *RSC Adv.* **2015**, *5*, 79593–79599. [CrossRef]

38. Wang, F.; Liu, H.; Hu, K.; Li, Y.; Zeng, W.; Zeng, L. Hierarchical Composites of MoS$_2$ Nanoflower Anchored on SnO$_2$ Nanofiber for Methane Sensing. *Ceram. Int.* **2019**, *45*, 22981–22986. [CrossRef]

39. Bai, J.; Shen, Y.; Zhao, S.; Chen, Y.; Li, G.; Han, C.; Wei, D.; Yuan, Z.; Meng, F. Flower-like MoS$_2$ Hierarchical Architectures Assembled by 2D Nanosheets Sensitized with SnO$_2$ Quantum Dots for High-Performance NH$_3$ Sensing at Room Temperature. *Sens. Actuators B Chem.* **2022**, *353*, 131191. [CrossRef]

40. Bai, X.; Lv, H.; Liu, Z.; Chen, J.; Wang, J.; Sun, B.; Zhang, Y.; Wang, R.; Shi, K. Thin-Layered MoS$_2$ Nanoflakes Vertically Grown on SnO$_2$ Nanotubes as Highly Effective Room-Temperature NO$_2$ Gas Sensor. *J. Hazard. Mater.* **2021**, *416*, 125830. [CrossRef]

41. Liu, A.; Lv, S.; Jiang, L.; Liu, F.; Zhao, L.; Wang, J.; Hu, X.; Yang, Z.; He, J.; Wang, C.; et al. The Gas Sensor Utilizing Polyaniline/MoS$_2$ Nanosheets/SnO$_2$ Nanotubes for the Room Temperature Detection of Ammonia. *Sens. Actuators B Chem.* **2021**, *332*, 129444. [CrossRef]

42. Wang, W.; Zhen, Y.; Zhang, J.; Li, Y.; Zhong, H.; Jia, Z.; Xiong, Y.; Xue, Q.; Yan, Y.; Alharbi, N.S.; et al. SnO$_2$ Nanoparticles-Modified 3D-Multilayer MoS$_2$ Nanosheets for Ammonia Gas Sensing at Room Temperature. *Sens. Actuators B Chem.* **2020**, *321*, 128471. [CrossRef]

43. Viet, N.N.; Thong, L.V.; Dang, T.K.; Phuoc, P.H.; Chien, N.H.; Hung, C.M.; Hoa, N.D.; Duy, N.V.; Toan, N.V.; Son, N.T.; et al. MoS$_2$ Nanosheets-Decorated SnO$_2$ Nanofibers for Enhanced SO$_2$ Gas Sensing Performance and Classification of CO, NH$_3$ and H$_2$ Gases. *Anal. Chim. Acta* **2021**, *1167*, 338576. [CrossRef] [PubMed]

44. Xu, X.; Liu, W.; Chen, Y.; Wang, S.; Wang, X.; Jiang, H.; Ma, S.; Yuan, F.; Zhang, Q. N-n Heterogeneous MoS$_2$/SnO$_2$ Nanotubes and The Excellent Triethylamine (TEA) Sensing Performances. *Mater. Lett.* **2022**, *311*, 131522. [CrossRef]

45. Han, Y.; Ma, Y.; Liu, Y.; Xu, S.; Chen, X.; Zeng, M.; Hu, N.; Su, Y.; Zhou, Z.; Yang, Z. Construction of MoS$_2$/SnO$_2$ Heterostructures for Sensitive NO$_2$ Detection at Room Temperature. *Appl. Surf. Sci.* **2019**, *493*, 613–619. [CrossRef]

46. Mirzaei, A.; Lee, M.H.; Pawar, K.K.; Bharath, S.P.; Kim, T.-U.; Kim, J.-Y.; Kim, S.S.; Kim, H.W. Metal Oxide Nanowires Grown by a Vapor–Liquid–Solid Growth Mechanism for Resistive Gas-Sensing Applications: An Overview. *Materials* **2023**, *16*, 6233. [CrossRef]

47. Kim, J.-H.; Mirzaei, A.; Kim, S.S.; Park, C. Pt Nanoparticle Decoration on Femtosecond Laser-Irradiated SnO$_2$ Nanowires for Enhancing C$_7$H$_8$ Gas Sensing. *Sens. Actuators B Chem.* **2023**, *379*, 133279. [CrossRef]

48. Li, Y.; Zhang, B.; Li, J.; Duan, Z.; Yang, Y.; Yuan, Z.; Jiang, Y.; Tai, H. Pd-Decorated ZnO Hexagonal Microdiscs for NH$_3$ Sensor. *Chemosensors* **2024**, *12*, 43. [CrossRef]

49. Shi, L.; Xu, Y.; Li, Q. Controlled Fabrication of SnO$_2$ Arrays of Well-Aligned Nanotubes and Nanowires. *Nanoscale* **2010**, *2*, 2104–2108. [CrossRef]

50. Mao, H.; Fu, Y.; Yang, H.; Deng, Z.; Sun, Y.; Liu, D.; Wu, Q.; Ma, T.; Song, X.-M. Ultrathin 1T-MoS$_2$ Nanoplates Induced by Quaternary Ammonium-Type Ionic Liquids on Polypyrrole/Graphene Oxide Nanosheets and Its Irreversible Crystal Phase Transition during Electrocatalytic Nitrogen Reduction. *ACS Appl. Mater. Interfaces* **2020**, *12*, 25189–25199. [CrossRef]

51. Wang, X.X.; Li, Z.; Yang, Y.; Tang, T.; Cheng, Y.F.; Xu, K.; Xie, H.G.; Chen, Y.L.; Cheng, L.; Tao, X.W.; et al. 3D Substoichiometric MoO$_{3-x}$/EGaln Framework for Room Temperature NH$_3$ Gas Sensing. *J. Alloys Compd.* **2023**, *939*, 168690. [CrossRef]

52. Hingangavkar, G.M.; Kadam, S.A.; Ma, Y.-R.; Bandgar, S.S.; Mulik, R.N.; Patil, V.B. MoS$_2$-GO Hybrid Sensor: A Discerning Approach for Detecting Harmful H$_2$S Gas at Room Temperature. *Chem. Eng. J.* **2023**, *472*, 144789. [CrossRef]

53. Rodrigues, J.; Jain, S.; Shimpi, N.G. Performance of 1D Tin (Sn) Decorated Spherical Shape ZnO Nanostructures as an Acetone Gas Sensor for Room and High Temperature. *Mater. Sci. Eng. B* **2023**, *288*, 116199. [CrossRef]

54. Kim, H.W.; Kwon, Y.J.; Mirzaei, A.; Kang, S.Y.; Choi, M.S.; Bang, J.H.; Kim, S.S. Synthesis of Zinc Oxide Semiconductors-Graphene Nanocomposites by Microwave Irradiation for Application to Gas Sensors. *Sens. Actuators B Chem.* **2017**, *249*, 590–601. [CrossRef]

55. Ma, X.; Cai, X.; Yuan, M.; Qu, Y.; Tan, Y.; Chen, F. Self-Powered and Flexible Gas Sensor Using Defect-Engineered WS_2/G Heterostructure. *Sens. Actuators B Chem.* **2022**, *371*, 132523. [CrossRef]

56. Choi, S.Y.; Kim, Y.; Chung, H.-S.; Kim, A.R.; Kwon, J.-D.; Park, J.; Kim, Y.L.; Kwon, S.-H.; Hahm, M.G.; Cho, B. Effect of Nb Doping on Chemical Sensing Performance of Two-Dimensional Layered $MoSe_2$. *ACS Appl. Mater. Interfaces* **2017**, *9*, 3817–3823. [CrossRef]

57. Guo, R.; Han, Y.; Su, C.; Chen, X.; Zeng, M.; Hu, N.; Su, Y.; Zhou, Z.; Wei, H.; Yang, Z. Ultrasensitive Room Temperature NO_2 Sensors Based on Liquid Phase Exfoliated WSe_2 Nanosheets. *Sens. Actuators B Chem.* **2019**, *300*, 127013. [CrossRef]

58. Wang, Z.; Zhang, T.; Zhao, C.; Han, T.; Fei, T.; Liu, S.; Lu, G. Rational Synthesis of Molybdenum Disulfide Nanoparticles Decorated Reduced Graphene Oxide Hybrids and Their Application for High-Performance NO_2 Sensing. *Sens. Actuators B Chem.* **2018**, *260*, 508–518. [CrossRef]

59. Ko, K.Y.; Park, K.; Lee, S.; Kim, Y.; Woo, W.J.; Kim, D.; Song, J.-G.; Park, J.; Kim, H. Recovery Improvement for Large-Area Tungsten Diselenide Gas Sensors. *ACS Appl. Mater. Interfaces* **2018**, *10*, 23910–23917. [CrossRef]

60. Chen, Z.; Wang, J.; Umar, A.; Wang, Y.; Li, H.; Zhou, G. Three-Dimensional Crumpled Graphene-Based Nanosheets with Ultrahigh NO_2 Gas Sensibility. *ACS Appl. Mater. Interfaces* **2017**, *9*, 11819–11827. [CrossRef]

61. Zhang, H.; Feng, J.; Fei, T.; Liu, S.; Zhang, T. SnO_2 Nanoparticles-Reduced Graphene Oxide Nanocomposites for NO_2 Sensing at Low Operating Temperature. *Sens. Actuators B Chem.* **2014**, *190*, 472–478. [CrossRef]

62. Liu, X.; Zhang, H.; Shen, T.; Sun, J. Flexible Resistive NO_2 Gas Sensor of SnO_2@$Ti_3C_2T_x$ MXene for Room Temperature Application. *Ceram. Int.* **2024**, *50*, 2459–2466. [CrossRef]

63. Liu, X.; Zhang, H.; Song, Y.; Shen, T.; Sun, J. Facile Solvothermal Synthesis of ZnO/$Ti_3C_2T_x$ MXene Nanocomposites for NO_2 Detection at Low Working Temperature. *Sens. Actuators B Chem.* **2022**, *367*, 132025. [CrossRef]

64. Yan, H.; Chu, L.; Li, Z.; Sun, C.; Shi, Y.; Ma, J. 2H-MoS_2/$Ti_3C_2T_x$ MXene Composites for Enhanced NO_2 Gas Sensing Properties at Room Temperature. *Sens. Actuators Rep.* **2022**, *4*, 100103. [CrossRef]

65. Ta, Q.T.H.; Tri, N.N.; Noh, J.S. Improved NO_2 Gas Sensing Performance of 2D MoS_2/$Ti_3C_2T_x$ MXene Nanocomposite. *Appl. Surf. Sci.* **2022**, *604*, 154624. [CrossRef]

66. Guo, F.; Feng, C.; Zhang, Z.; Zhang, L.; Xu, C.; Zhang, C.; Lin, S.; Wu, H.; Zhang, B.; Tabusi, A.; et al. A Room-Temperature NO_2 Sensor Based on $Ti_3C_2T_X$ MXene Modified with Sphere-Like CuO. *Sens. Actuators B Chem.* **2023**, *375*, 132885. [CrossRef]

67. Premkumar, V.K.; Vishnuraj, R.; Sheena, T.S.; Yang, X.; Pullithadathil, B.; Zhang, C.; Wu, Z. Influence of ZnO Hexagonal Pyramid Nanostructures for Highly Sensitive and Selective NO_2 Gas Sensor. *J. Alloys Compd.* **2024**, *994*, 174625. [CrossRef]

68. Kim, J.-H.; Mirzaei, A.; Kim, H.W.; Kim, S.S. Low Power-Consumption CO Gas Sensors Based on Au-Functionalized SnO_2-ZnO Core-Shell Nanowires. *Sens. Actuators B Chem.* **2018**, *267*, 597–607. [CrossRef]

69. Babar, B.M.; Pisal, K.B.; Mujawar, S.H.; Patil, V.L.; Kadam, L.D.; Pawar, U.T.; Kadam, P.M.; Patil, P.S. Concentration Modulated Vanadium Oxide Nanostructures for NO_2 Gas Sensing. *Sens. Actuators B Chem.* **2022**, *351*, 130947. [CrossRef]

70. Sharma, A.; Tomar, M.; Gupta, V. A Low Temperature Operated NO_2 Gas Sensor Based on TeO_2/SnO_2 p–n Heterointerface. *Sens. Actuators B Chem.* **2013**, *176*, 875–883. [CrossRef]

71. Bang, J.H.; Choi, M.S.; Mirzaei, A.; Kwon, Y.J.; Kim, S.S.; Kim, T.W.; Kim, H.W. Selective NO_2 Sensor Based on Bi_2O_3 Branched SnO_2 Nanowires. *Sens. Actuators B Chem.* **2018**, *274*, 356–369. [CrossRef]